Nuclear Science and Techniques (2025) 36:45
https://doi.org/10.1007/s41365-024-01607-x

A perspective on describing nucleonic flow and pionic observables within the ultra-relativistic quantum molecular dynamics model

Yang-Yang Liu[1] · Jun-Ping Yang[1] · Yong-Jia Wang[2] · Qing-Feng Li[2,3] · Zhu-Xia Li[1] · Cheng-Jun Xia[4] · Ying-Xun Zhang[1,5]

Received: 30 May 2024 / Revised: 8 September 2024 / Accepted: 16 September 2024 / Published online: 29 January 2025

Abstract
In this work, we study the impacts of the isospin-independent momentum-dependent interaction (MDI) and near-threshold $NN \to N\Delta$ cross sections ($\sigma_{NN\to N\Delta}$) on the nucleonic flow and pion production observables in the ultra-relativistic quantum molecular dynamics (UrQMD) model. With the updated isospin-independent MDI and the near-threshold $NN \to N\Delta$ cross sections in the UrQMD model, 17 observables, which are the directed flow (v_1) and elliptic flow (v_2) of neutrons, protons, Hydrogen (H), and charged particles as a function of transverse momentum (p_t/A) or normalized rapidity (y_0^{lab}), and the observables constructed from them, the charged pion multiplicity ($M(\pi)$) and its ratio ($M(\pi^-)/M(\pi^+)$), can be simultaneously described at certain forms of symmetry energy. The refinement of the UrQMD model provides a solid foundation for further understanding the effects of the missed physics, such as the threshold effect, the pion potential, and the momentum-dependent symmetry potential. Circumstantial constraints on the symmetry energy at the flow characteristic density $1.2 \pm 0.6\rho_0$ and the pion characteristic density $1.5 \pm 0.5\rho_0$ were obtained with the current version of UrQMD, and the corresponding symmetry energies were $S(1.2\rho_0) = 34 \pm 4\,\mathrm{MeV}$ and $S(1.5\rho_0) = 36 \pm 8\,\mathrm{MeV}$, respectively. Furthermore, the discrepancies between the data and the calculated results of v_2^{n} and v_2^{p} at high p_t (rapidity) imply that the roles of the missing ingredients, such as the threshold effect, the pion potential, and the momentum-dependent symmetry potential, should be investigated by differential observables, such as the momentum and rapidity distributions of the nucleonic and pionic probes over a wide beam energy range.

Keywords Momentum dependent interaction · $NN \to N\Delta$ cross section · Symmetry energy · Flow and π observable

This work was supported by the National Natural Science Foundation of China (Nos. 11875323, 12275359, 12205377, 12335008, U2032145, 11790320, 11790323, 11790325, and 11961141003), the National Key R&D Program of China (No. 2018 YFA0404404), the Continuous Basic Scientific Research Project (No. WDJC-2019-13), the China Institute of Atomic Energy (No. YZ222407001301), and the Leading Innovation Project of the CNNC (Nos. LC192209000701 and LC202309000201).

✉ Ying-Xun Zhang
zhyx@ciae.ac.cn

Yang-Yang Liu
liuyangyang@ciae.ac.cn

Yong-Jia Wang
wangyongjia@zjhu.edu.cn

Qing-Feng Li
liqf@zjhu.edu.cn

1 China Nuclear Data Center, China Institute of Atomic Energy, Beijing 102413, China

1 Introduction

The isospin asymmetric nuclear equation of state is crucial for understanding isospin-asymmetric objects such as the structure of neutron-rich nuclei, the mechanism of neutron-rich heavy ion collisions (HICs), and the properties

2 School of Science, Huzhou University, Huzhou 313000, China

3 Institute of Modern Physics, Chinese Academy of Sciences, Lanzhou 730000, China

4 Center for Gravitation and Cosmology, College of Physical Science and Technology, Yangzhou University, Yangzhou 225009, China

5 Guangxi Key Laboratory of Nuclear Physics and Technology, Guangxi Normal University, Guilin 541004, China

of neutron stars, including neutron star mergers and core-collapse supernovae [1–10]. The symmetric part of the isospin-asymmetric equation of state has been well constrained using flow and kaon condensation [11]. However, the symmetry energy away from the normal density still has a large uncertainty, making the constraint of symmetry energy becomes one of the important goals in nuclear physics [12, 13].

For probing the symmetry energy at suprasaturation density using HICs, the isospin-sensitive observables, such as the ratio of elliptic flow of neutrons to charged particles, hydrogen isotopes, or protons ($v_2^{\rm n}/v_2^{\rm ch}$, $v_2^{\rm n}/v_2^{\rm H}$, or $v_2^{\rm n}/v_2^{\rm p}$) [14–18] and the multiplicity ratio of charged pions (i.e., $M(\pi^-)/M(\pi^+)$ or denoted as π^-/π^+) [19–30], were mainly used. By comparing the calculations with transverse momentum-dependent or integrated elliptic flow data of nucleons, hydrogen isotopes, and charged particles from the FOPI/LAND and ASY-EOS experimental collaborations, a moderately soft to linear symmetry energy was obtained with the UrQMD [14, 16, 31] and Tübingen quantum molecular dynamics (TüQMD) model [15, 18]. The lower limit of L obtained from the flow ratio data is $L > 60\,\mathrm{MeV}$ [32], which overlaps with the upper limits of the constraints from the nuclear structure and isospin diffusion, i.e., $L \approx 60 \pm 20\,\mathrm{MeV}$ [33–35]. It shows strong model dependence for the symmetry energy constraints from π^-/π^+ [21–23, 25–28, 36] and the extracted value of L ranges from 5 to 144 MeV. This may be due to the different treatments of nucleonic potential, Δ potential, threshold effects, pion potential, Pauli blocking, in-medium cross sections, and by using the different numerical techniques for solving transport equations.

To understand the model dependence of the symmetry energy constraints of HICs and improve it in the future, two aspects should be considered. One is to find and fix the deficiencies of transport models, which can be achieved through a transport model evaluation project. The other is to test the model by simultaneously describing the multi-observable data and then providing the constraints of symmetry energy at their probed densities.

The transport model evaluation project has made important progress in benchmarking the treatment of particle-particle collision [37, 38] and nucleonic mean field potential [39] in both the Boltzmann-Uehling-Uhlenbeck (BUU) type and quantum molecular dynamics (QMD) type models. In the collision part, a time-step-free method is suggested [37, 38] for simulating the collisions or decay of resonance particles because it automatically determines whether the resonance will collide or decay according to the sequence of the collision time and decay time. In the UrQMD model, the time-step-free method is adopted in the collision part [37, 38], and the nucleonic potential is also involved in extending its application to low-intermediate energy HICs [16, 28].

Despite the successful applications of the UrQMD model in studying heavy-ion collisions (HICs) across a range of energies from low-intermediate to high energy [16, 28, 32, 40, 41], previous calculations have revealed that the data of pion multiplicity and the nucleonic flow observables for Au+Au at 0.4A GeV were not simultaneously described. This 'inconsistency' may be attributed to the momentum-dependent interaction (MDI) form and near-threshold $\sigma_{NN\to N\Delta}$ cross sections used in the UrQMD model [16, 28].

The MDI form used in the previous analyses on the elliptic flow of neutrons, protons, hydrogen isotopes, charged particles [16] or the pion multiplicity [28] is $t_4 \ln^2(1 + t_5(\mathbf{p}_1 - \mathbf{p}_2)^2)\delta(\mathbf{r}_1 - \mathbf{r}_2)$, in which the MDI parameters were extracted by fitting the Arnold's optical potential data [42]. By using this MDI form in the UrQMD, the transverse momentum-dependent elliptic flow for neutrons and hydrogen isotopes is underestimated by 40% in the high p_t/A region [31]. In the 1990 s, the real part of the global Dirac optical potential (Schrodinger equivalent potential) was published by Hama et al. [43], in which the angular distribution and polarization quantities in proton-nucleus elastic scattering in the 10 MeV to 1 GeV range were analyzed. Based on Hama's data, a Lorentzian-type momentum-dependent interaction [44] was generated and used in the IQMD model in Ref. [44], and in many versions of transport model, such as the Boltzmann-Nordheim-Vlasov (BNV) [45], IBUU [46–48], the jet AA microscopic transportation model + relativistic version of the QMD model (JAM+RQMD) [49], previous version of the UrQMD [50], the Giessen-BUU model (GiBUU) [51], the antisymmetrized molecular dynamics approach (AMD) +JAM [52], RQMD [53], TüQMD [54] model for studying intermediate-high energy HICs. The MDI [44] generated from Hama's data provides a stronger momentum-dependent potential than that from Arnold's data in the high-momentum region. Thus, checking whether Hama's MDI form can refine the nucleonic flow description in the UrQMD model is important.

For the cross sections of the $NN \to N\Delta$ channel used in the UrQMD model, they are obtained by fitting CERN8401 data [55]. This fitting formula underestimates the data for $\sigma_{NN\to N\Delta}$ near the threshold energy, which will be shown in Fig. 2 in Sect. 2, and thus leads to an underestimation of the pion productions in the UrQMD calculation. The other transport models, such as TüQMD, pBUU, and RVUU, use the $\sigma_{NN\to N\Delta}$ cross section obtained from the one-boson exchange model by fitting CERN8301 data. However, one should note that the data from CERN8301 and CERN8401 were different, particularly near the threshold energy. Thus, investigations of the different formulas of $\sigma_{NN\to N\Delta}$ near the threshold energy are necessary for describing the pion observables.

Another method for reducing model uncertainties is to simultaneously describe the multi-observables data (or doing so-called combination analysis), including the isospin-independent and isospin-dependent nucleonic collective flow and pion observables. For the combination analysis on the isospin sensitive nucleonic flow and pion observables, there were few works to simultaneously investigate them, except for the TüQMD model [27] and IBUU model [17]. In the TüQMD model, the medium correction on the cross sections, energy conservation, and momentum-dependent symmetry potential have been considered, and four observables, such as M_{π^+}, M_{π^-}, π^-/π^+, and integral $v_2^{\rm n}/v_2^{\rm p}$, were analyzed. In the IBUU model, the nucleon-nucleon short-range correlations and isospin-dependent in-medium inelastic baryon-baryon scattering cross sections were considered, and six integrated flow and pion observables were analyzed.

In the last decades, ASY-EOS, FOPI-LAND, and FOPI have published 17 datasets on nucleonic collective flows and pion observables, as listed in Table 3, which provides a significant opportunity to benchmark the model and understand the contributions of the different physical phenomena. In this study, we attempted to use 17 observables to limit the physical uncertainties and improve the ability of the UrQMD model.

The paper is organized as follows: In Sect. 2, we briefly introduce the MDI, symmetry energy, and $\sigma_{NN\rightarrow N\Delta}$ that will be refined in the UrQMD model. In Sect. 3, the impacts of MDI, symmetry energy, and the refined $\sigma_{NN\rightarrow N\Delta}$ on the 17 observables, such as nucleonic flow and pion observables, are presented and discussed. In Sect. 4, the symmetry energy constraints at the flow and pion characteristic densities are obtained and the model dependence of them are discussed. Section 5 concludes this study.

2 UrQMD model and its refinements

The UrQMD model version we used is the same as that used in Ref. [28], in which the cross sections of the $N\Delta \rightarrow NN$ channel are replaced with a more delicate form by considering the Δ-mass dependence of the M-matrix in the calculation of the $N\Delta \rightarrow NN$ cross section [56]. This differs from the version used to describe only the flow data and constraints in Refs. [16, 32]. To distinguish them, we named the current version as UrQMD-CIAE and previous version as UrQMD-HZU. The main differences are the momentum dependence potential and $NN \leftrightarrow N\Delta$ cross section.

We focused on the impacts of different forms of the MDI, symmetry energy, and $\sigma_{NN\rightarrow N\Delta}$ and have briefly introduced them in the subsequent sections. The nucleonic potential energy U was calculated from the potential energy density u, i.e., $U = \int u \mathrm{d}^3 r$. The u reads as

$$
\begin{aligned}
u =& \frac{\alpha}{2}\frac{\rho^2}{\rho_0} + \frac{\beta}{\eta+1}\frac{\rho^{\eta+1}}{\rho_0^{\eta}} \\
&+ \frac{g_{\rm sur}}{2\rho_0}(\nabla\rho)^2 + \frac{g_{\rm sur,iso}}{\rho_0}[\nabla(\rho_{\rm n}-\rho_{\rm p})]^2 \\
&+ u_{\rm md} + u_{\rm sym}.
\end{aligned} \tag{1}
$$

The parameters α, β, and η are related to the two and nonlinear density-dependent interaction term. The third and fourth terms are the isospin-independent and isospin-dependent surface term, respectively. The $u_{\rm md}$ is from the MDI term, and two forms were adopted in this work. $u_{\rm sym}$ denotes the symmetry potential energy term.

The energy density associated with the MDI, i.e., $u_{\rm md}$, is calculated according to the following relationship:

$$
u_{\rm md} = \sum_{ij} \int d^3p_1 d^3p_2 f_i(\vec{r},\vec{p}_1) f_j(\vec{r},\vec{p}_2) v_{\rm md}(\Delta p_{12}). \tag{2}
$$

$f_i(\vec{r},\vec{p}_1)$ denotes the phase space density of nucleon i. The MDI form, that is, $v_{\rm md}(\Delta p_{12})$, is assumed to be

$$
v_{\rm md}(\Delta p_{12}) = t_4 \ln^2(1 + t_5 \Delta p_{12}^2) + c, \tag{3}
$$

where $\Delta p_{12} = |\mathbf{p}_1 - \mathbf{p}_2|$, and the parameters t_4, t_5, and c are obtained by fitting the data of the real part of the optical potential. In detail, we fit the data of the real part of the nucleon-nucleus optical potential $V_{\rm md}(p_1)$ according to the following ansatz:

$$
V_{\rm md}(p_1) = \int_{p_2<p_F} v_{\rm md}(p_1 - p_2) \mathrm{d}^3 p_2 \Big/ \int_{p_2<p_{\rm F}} \mathrm{d}^3 p_2. \tag{4}
$$

This method is the same as that used in Ref. [44].

Two sets of the real part of optical potential data were used in this work. One is from Arnold et al. [42], which was used in the previous version of the UrQMD model [16, 28]. Another is from Hama et al. [43], which is widely used in many transport models, such as BNV [45], IBUU [46–48], JAM+RQMD [49], the previous version of the UrQMD [50], GiBUU [51], AMD +JAM [52], RQMD [53], and the TüQMD [54] model. The momentum dependence of $v_{\rm md}^{\rm Hama}(\Delta p_{12})$ is stronger than that of $v_{\rm md}^{\rm Arnold}(\Delta p_{12})$, and the value of $v_{\rm md}^{\rm Hama}(\Delta p_{12})$ is larger than that of $v_{\rm md}^{\rm Arnold}(\Delta p_{12})$ at high momentum region. The corresponding single-particle potentials are presented in Fig. 1a. Because the MDI can influence the EOS, parameters α, β, and η should be readjusted to keep the desired shape. The parameters α, β, and η were readjusted to maintain the incompressibility of the symmetric nuclear matter $K_0 = 231$ MeV for the two different MDIs, and the values of the parameters and the corresponding effective mass m^*/m are listed in Table 1.

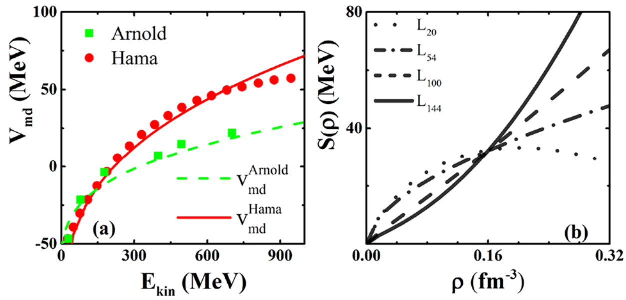

Fig. 1 (Color online) **a** The parametrization of the bare interaction v_{md} (lines) as compared to the data points of the real part of optical potential (symbols) from Arnold et al. [42] (green) and Hama et al. [43] (red). **b** Density dependence of the symmetry energy with different S_0 and L values

For the potential energy density of the symmetry energy part, i.e., u_{sym}, only the local interaction has contribution since the nonlocal term is isospin-independent momentum dependent interaction. We take two forms of u_{sym}^{pot} in our calculations: the Skyrme-type polynomial form ((a) in Eq. (5)) and the density power law form ((b) in Eq. (5)), which read as

$$u_{sym} = S_{sym}^{pot}(\rho)\rho\delta^2 = \begin{cases} (A(\frac{\rho}{\rho_0}) + B(\frac{\rho}{\rho_0})^{\gamma_s} + C(\frac{\rho}{\rho_0})^{5/3})\rho\delta^2, & \textbf{(a)} \\ \frac{C_s}{2}(\frac{\rho}{\rho_0})^{\gamma_i}\rho\delta^2. & \textbf{(b)} \end{cases} \quad (5)$$

Correspondingly, the density dependence of the symmetry energy is

$$S(\rho) = \frac{\hbar^2}{6m}\left(\frac{3\pi^2\rho}{2}\right)^{2/3} + S_{sym}^{pot}(\rho). \quad (6)$$

In Eq. (5), A, B, C, C_s, and γ_i are the parameters of the symmetry potential directly used in the UrQMD model. They are determined by the symmetry energy values at the saturation density S_0, the slope of the symmetry energy L, and the parameters in Table 1 according to the relationship described in Refs. [35, 57], where $S_0 = S(\rho_0)$ and $L = 3\rho_0 \partial S(\rho)/\partial\rho|_{\rho_0}$. The ranges of S_0 and L are listed in Table 2. In this work, we varied S_0 and L to investigate the influence of the symmetry energy on HIC observables.

Table 2 Parameters of symmetry energy and effective mass used in the calculations

Para. name	Values	Description
S_0	[30, 34]	Symmetry energy coefficient
L	[5,144]	Slope of symmetry energy
m^*/m	0.635,0.77	Isoscalar effective mass

For the $L < 35$ MeV case, we used the Skyrme-type polynomial form of $S_{sym}^{pot}(\rho)$ because the simple power law form of the symmetry energy cannot provide reasonable values at the subnormal density. Furthermore, the $L < 5$ MeV sets are not adopted because the corresponding symmetry energy becomes negative at densities above $2.7\rho_0$ and the EOS is not favored by the neutron star properties. Thus, the lower limit of L in our calculations was 5 MeV. For $L > 35$ MeV, we used a simple power law form of $S_{sym}^{pot}(\rho)$. As an example, we present the density dependence of the symmetry energy in Fig. 1b for $L = 20$, 144 MeV at $S_0 = 30$ and 34 MeV.

The symmetry potential of Δ resonance was calculated from the symmetry potential of the nucleon as same as that in Refs. [20, 22, 26–28, 58, 59]. The effects of different strengths of Δ potential on pion production were also investigated in Refs. [28, 60], and the total and differential π^-/π^+ ratios in heavy ion collisions above the threshold energy were weakly influenced by the completely unknown symmetry (isovector) potential of the Δ(1232) resonance, owing to the very short lifetimes of the Δ resonances.

In the collision term, medium-modified nucleon-nucleon elastic cross sections were used, as same as that in our previous works [32]. For the $NN \to N\Delta$ cross sections used in UrQMD [40], a formula used to fit the CERN8401 data was adopted and denoted as $\sigma_{NN\to N\Delta}^{UrQMD}$. After zooming out the figure of the $NN \to N\Delta$ cross sections near the threshold in Ref. [40], we found that $\sigma_{NN\to N\Delta}^{UrQMD}$ underestimated the data [55] by approximately 3 mb at $E = 0.4A$ GeV. This discrepancy is illustrated in Fig. 2a, where the blue line is the default fitting formula in Ref. [40] and the solid symbols represent the CERN8401 data obtained from Ref. [55]. One can expect that the default formula $\sigma_{NN\to N\Delta}^{UrQMD}$ would underestimate the pion multiplicities. Thus, we used an accurate form of $\sigma_{NN\to N\Delta}$ near the threshold energy to

Table 1 Parameters used in the present work

Para	t_4	t_5	c	α	β	η	K_0	m^*/m
v_{md}^{Arnold}	1.57	5×10^{-4}	− 54	− 221	153	1.31	231	0.77
v_{md}^{Hama}	3.058	5×10^{-4}	− 86	− 335	253	1.16	231	0.635

t_4, c, α, β and K_0 are in MeV. t_5 is in MeV^{-2}, and η and m^*/m are dimensionless. The Gaussian wave packet width is taken as 1.414 fm for Au+Au collision

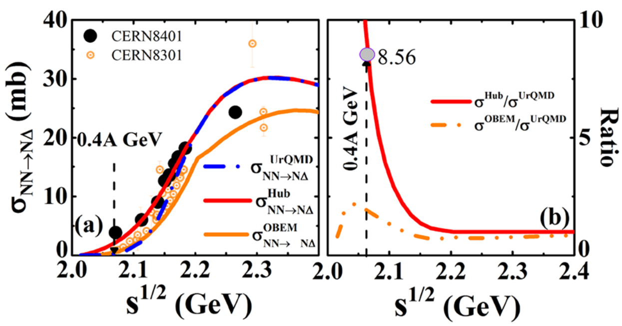

Fig. 2 (Color online) **a** The $NN \to N\Delta$ cross section with default parameterization in the UrQMD model $\sigma^{\mathrm{UrQMD}}_{NN\to N\Delta}$(blue line), Hubbert parameterization $\sigma^{\mathrm{Hub}}_{NN\to N\Delta}$ (red line), and that obtained based on the OBE model $\sigma^{\mathrm{OBEM}}_{NN\to N\Delta}$[61] (orange line). **b** The ratio of $\sigma^{\mathrm{Hub}}_{NN\to N\Delta}$ over $\sigma^{\mathrm{UrQMD}}_{NN\to N\Delta}$ (red line) and $\sigma^{\mathrm{OBEM}}_{NN\to N\Delta}$ over $\sigma^{\mathrm{UrQMD}}_{NN\to N\Delta}$ (orange line) as a function of energy $\sqrt{s}$

describe pion production at 0.4A GeV. A Hubbert function form was used to refit the $NN \to N\Delta$ cross sections data at $\sqrt{s} < 2.21$ GeV. That is,

$$\sigma_{NN\to N\Delta}(\sqrt{s}) = A_1 + \frac{4A_2 \times e^{-(\sqrt{s}-A_3)/A_4}}{(1+e^{-(\sqrt{s}-A_3)/A_4})^2}, \quad \sqrt{s} < 2.21\,\mathrm{GeV}. \tag{7}$$

In which, $A_1 = -1.11$ mb, $A_2 = 26.30$ mb, $A_3 = 2.24$ GeV, and $A_4 = 0.05$ GeV. We denote this as $\sigma^{\mathrm{Hub}}_{NN\to N\Delta}$ to distinguish it from the default form in Ref. [40]. The fitting result is represented by red line in Fig. 2a. Above 2.21 GeV, the default fitting function was used.

As shown in Fig. 2a, the $\sigma^{\mathrm{Hub}}_{NN\to N\Delta}$ is closer to the experimental data than the $\sigma^{\mathrm{UrQMD}}_{NN\to N\Delta}$. The right panel shows that the ratio of $R = \sigma^{\mathrm{Hub}}_{NN\to N\Delta}/\sigma^{\mathrm{UrQMD}}_{NN\to N\Delta}$, and one can see that the cross section $\sigma^{\mathrm{Hub}}_{NN\to N\Delta}$ increases by a factor of 8.56 at a beam energy of 0.4A GeV. Consequently, one can expect a higher pion multiplicity with $\sigma^{\mathrm{Hub}}_{NN\to N\Delta}$ than the one with $\sigma^{\mathrm{UrQMD}}_{NN\to N\Delta}$.

Additionally, we present another form of $\sigma_{NN\to N\Delta}$ (indicated by the orange line in Fig. 2a), which has been widely used in the other transport models [23, 27, 30, 54, 58]. This was obtained by fitting the results from the one-boson exchange model [61], in which the model parameters were obtained by fitting the CERN8301 experimental data [62], referred to as $\sigma^{\mathrm{OBEM}}_{NN\to N\Delta}$ in this work. At 0.4A GeV, the data from CERN8301 was smaller than the one from CERN8401, and the difference between the data from CERN8301 and CERN8401 was approximately 3 mb. Correspondingly, the ratio $R = \sigma^{\mathrm{OBEM}}_{NN\to N\Delta}/\sigma^{\mathrm{UrQMD}}_{NN\to N\Delta}$ decreased to 1.88, and one can expect that the pion multiplicity will be underestimated in transport models with this form. To enhance the pion multiplicity in the transport model calculations, the threshold effects may needed when the $\sigma^{\mathrm{OBEM}}_{NN\to N\Delta}$ is used in the model.

For the $N\Delta \to NN$ cross sections, they were obtained based on the detailed balance, in which the Δ mass-dependent $N\Delta \to NN$ cross sections were also considered as in Refs. [28, 56].

3 The descriptions of the collective flow and pion observables

The collective flow reflects the directional features of the transverse collective motion, which can be quantified in terms of the moments of the azimuthal angle relative to the reaction plane, i.e., $v_n = \langle\cos(n\phi)\rangle$, $n = 1, 2, 3, \cdots$. Among the v_n, the elliptic flow v_2 has been used to determine the MDI [63], and the elliptic flow ratios, such as $v_2^{\mathrm{n}}/v_2^{\mathrm{p}}$, $v_2^{\mathrm{n}}/v_2^{\mathrm{H}}$, and $v_2^{\mathrm{n}}/v_2^{\mathrm{ch}}$ are proposed to determine the symmetry energy at suprasaturation density [16, 18, 31]. Pions are known to be mainly produced through Δ resonance decay in the suprasaturation density region at an early stage, and the multiplicity ratio of charged pions, i.e., π^-/π^+, is also considered as a probe for constraining the symmetry energy at the suprasaturation density and has been widely studied [19–23, 27, 28].

In this work, we perform the calculations of Au+Au collision at 0.4A GeV with UrQMD model, and 200,000 events are simulated for each impact parameter. The final flow observables as functions of p_t/A and y_0^{lab} are obtained by integrating over b with a Gaussian weight. For the one with p_t/A, the integration range is b from 0 to 10 fm [31, 64–66]; for the one with y_0^{lab}, it is from 5 to 7 fm. The pion observable was also obtained by integrating over b from 0 to 2 fm with a certain weight, which is the same as that in Ref. [67]. The 17 observables listed in Table 3 are investigated in the following analysis.

3.1 Directed flow and elliptic flow

Figure 3a and b shows the directed flow as a function of the transverse momentum per particle p_t/A for neutrons $v_1^{\mathrm{n}}(p_t/A)$ and for charged particles $v_1^{\mathrm{ch}}(p_t/A)$ at given rapidity regions and angle cuts. The symbols represent the ASY-EOS data from Ref. [31]. The lines correspond to UrQMD calculations using $v_{\mathrm{md}}^{\mathrm{Arnold}}$ (green) and $v_{\mathrm{md}}^{\mathrm{Hama}}$ (blue and red) for the $L = 144$ MeV (solid lines) and $L = 20$ MeV (dashed lines) cases at $S_0 = 32.5$ MeV. In which, green and blue lines correspond to $\sigma^{\mathrm{UrQMD}}_{NN\to N\Delta}$, and red lines correspond to $\sigma^{\mathrm{Hub}}_{NN\to N\Delta}$. By comparing the green and blue lines, the effects of MDI can be understood, while the comparison between blue and red lines can be used to study the effects of $\sigma_{NN\to N\Delta}$. The calculations show that $v_1^{\mathrm{n}}(p_t/A)$ and $v_1^{\mathrm{ch}}(p_t/A)$ increase from

Table 3 Status of transport models for describing 17 experimental observables from the published papers

Observable	Experimental data	IBUU	IBL	LQMD	pBUU	RVUU	χBUU	TüQMD	UrQMD-HZU	UrQMD-CIAE
$v_1^{\mathrm{n}}(p_{\mathrm{t}}/A)$	ASY-EOS[31]	–	–	–	–	–	–	–	+[31]	+
$v_2^{\mathrm{n}}(p_{\mathrm{t}}/A)$	ASY-EOS[31]	–	–	–	–	–	–	+[18]	+[31]	+
$v_1^{\mathrm{ch}}(p_{\mathrm{t}}/A)$	ASY-EOS[31]	–	–	–	–	–	–	–	+[31]	+
$v_2^{\mathrm{ch}}(p_{\mathrm{t}}/A)$	ASY-EOS[31]	–	–	–	–	–	–	+[18]	+[31]	+
$v_2^{\mathrm{n}}/v_2^{\mathrm{ch}}(p_{\mathrm{t}}/A)$	ASY-EOS[31]	–	–	–	–	–	–	+[18]	+[31]	+
$v_2^{\mathrm{n}}(p_{\mathrm{t}}/A)$	FOPI-LAND[14]	–	–	–	–	–	–	+[18]	+[14]	+
$v_2^{\mathrm{H}}(p_{\mathrm{t}}/A)$	FOPI-LAND[14]	–	–	–	–	–	–	+[18]	+[14]	+
$v_2^{\mathrm{n}}(y_0^{\mathrm{lab}})$	FOPI-LAND[14]	+[17]	–	–	–	–	–	+[18]	+[14]	+
$v_2^{\mathrm{P}}(y_0^{\mathrm{lab}})$	FOPI-LAND[14]	+[17]	–	–	–	–	–	+[18]	–	+
$v_2^{\mathrm{n}}/v_2^{\mathrm{H}}(p_{\mathrm{t}}/A)$	FOPI-LAND[14]	–	–	–	–	–	–	+[18]	+[16]	+
$v_2^{\mathrm{n}}/v_2^{\mathrm{P}}(y_0^{\mathrm{lab}})$	FOPI-LAND[14]	–	–	–	–	–	–	+[18]	–	+
$v_2^{\mathrm{n}}/v_2^{\mathrm{H}}$	FOPI-LAND[14]	–	–	–	–	–	–	+[18]	+[16]	+
$v_2^{\mathrm{n}}/v_2^{\mathrm{P}}$	FOPI-LAND[14]	+[17]	–	–	–	–	–	+[18]	+[16]	+
$v_2^{\mathrm{n}}-v_2^{\mathrm{H}}$	FOPI-LAND[14]	–	–	–	–	–	–	–	+[16]	+
$v_2^{\mathrm{n}}-v_2^{\mathrm{P}}$	FOPI-LAND[14]	–	–	–	–	–	–	–	+[16]	+
$M(\pi)$	FOPI[67]	+ [17, 21]	+[23]	+[22]	+[25]	+[26, 70]	+[79]	+[27]	–	+[28]
π^-/π^+	FOPI[67]	+ [17, 21]	+[23]	+[22]	+[25]	+[26, 70]	+[79]	+[27]	–	+[28]

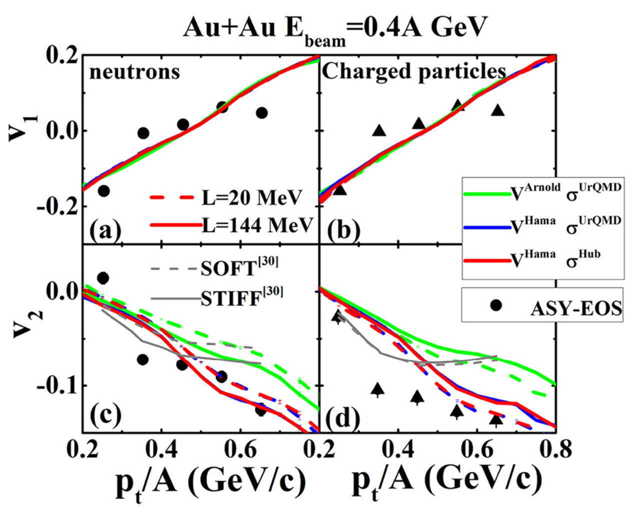

Fig. 3 (Color online) **a** $v_1(p_t/A)$ for neutrons; **b** $v_1(p_t/A)$ for charged particles; **c** $v_2(p_t/A)$ for neutrons, and **d** $v_2(p_t/A)$ for charged particles for ^{197}Au+^{197}Au collisions. The dash and solid lines correspond to the results with $L = 20$ MeV and $L = 144$ MeV at $S_0 = 32.5$ MeV, respectively. The gray lines are the results in Ref. [31]. The black symbols are ASY-EOS data[31]

negative to positive as p_t/A increases, and the sign of v_1 changes around $p_t/A \approx 0.5$ GeV/c. Furthermore, the calculations show that there are no sensitivities of v_1 to L, MDI, and $\sigma_{NN\to N\Delta}$ in the selected rapidity region owing to the spectator matter-blocking effect. In addition, calculations with different combinations of L, MDI, and $\sigma_{NN\to N\Delta}$ fall within this data region.

Figure 3c and d shows the elliptic flow of neutrons $v_2^{\mathrm{n}}(p_{\mathrm{t}}/A)$ and charged particles $v_2^{\mathrm{ch}}(p_{\mathrm{t}}/A)$, with different L, MDI, and $\sigma_{NN\to N\Delta}$. The symbols and lines have the same meaning as in panels (a) and (b), respectively. The gray lines represent the results in Ref. [31]. Both v_2^{n} and v_2^{ch} have negative values and decrease as p_{t}/A increases, indicating a preference for particle emission out of the reaction plane toward 90 and 270°. Notably, both v_2^{n} and v_2^{ch} at high p_{t} regions are highly sensitive to the strength of MDI and L but are hardly influenced by the forms of $\sigma_{NN\to N\Delta}$. This is because only 6% of NN collisions belong to $NN \to N\Delta$ collisions in the presently studied beam energy [28]. The values of v_2 obtained with $v_{\mathrm{md}}^{\mathrm{Hama}}$ are always lower than those obtained with $v_{\mathrm{md}}^{\mathrm{Arnold}}$ because the momentum dependence of $v_{\mathrm{md}}^{\mathrm{Hama}}$ is stronger than that of $v_{\mathrm{md}}^{\mathrm{Arnold}}$. The calculations of v_2^{n} and v_2^{ch} with $v_{\mathrm{md}}^{\mathrm{Hama}}$ are closer to the ASY-EOS experimental data than those obtained using the previous version of UrQMD [31] (gray lines), in which $v_{\mathrm{md}}^{\mathrm{Arnold}}$ is used.

In addition to MDI, the v_2^{n} and v_2^{ch} both exhibit some sensitivity to the stiffness of the symmetry energy. As shown in Fig. 3c, the values of v_2^{n} obtained with the $L = 144$ MeV (stiff) case are lower than those obtained with the $L = 20$ MeV (soft) case. This is because the stiff symmetry energy provides a stronger repulsive force on the neutrons at suprasaturation density than that with the soft symmetry energy case. For charged particles, as shown in panel (d), the v_2^{ch} obtained in the stiff symmetry energy case is higher

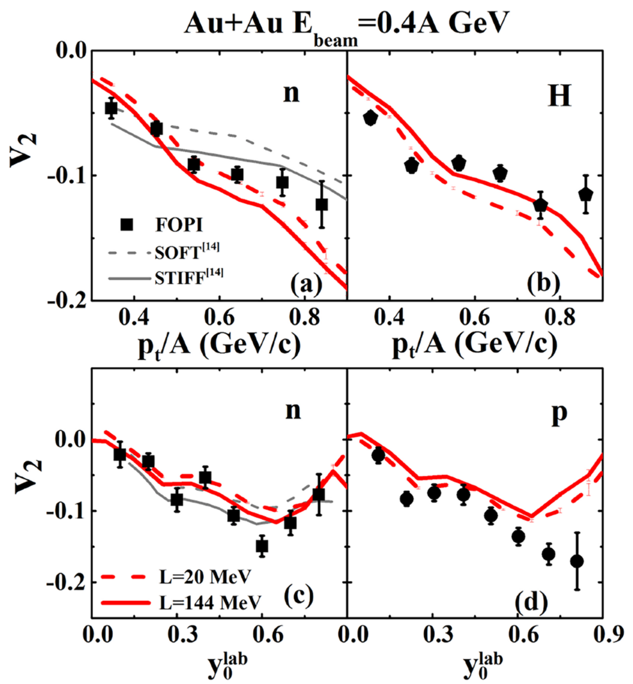

Fig. 4 **a** $v_2(p_t/A)$ for neutrons; **b** $v_2(p_t/A)$ for H isotopes; **c** $v_2(y_0^{lab})$ for neutrons; and **d** $v_2(y_0^{lab})$ for protons for ^{197}Au+^{197}Au collisions. The red lines are for $V_{\mathrm{md}}^{\mathrm{Hama}}$ and $\sigma_{NN\to N\Delta}^{\mathrm{Hub}}$ at $S_0 = 32.5$ MeV. The gray lines are the results in Ref. [14], and the black symbols are the FOPI-LAND data[14]

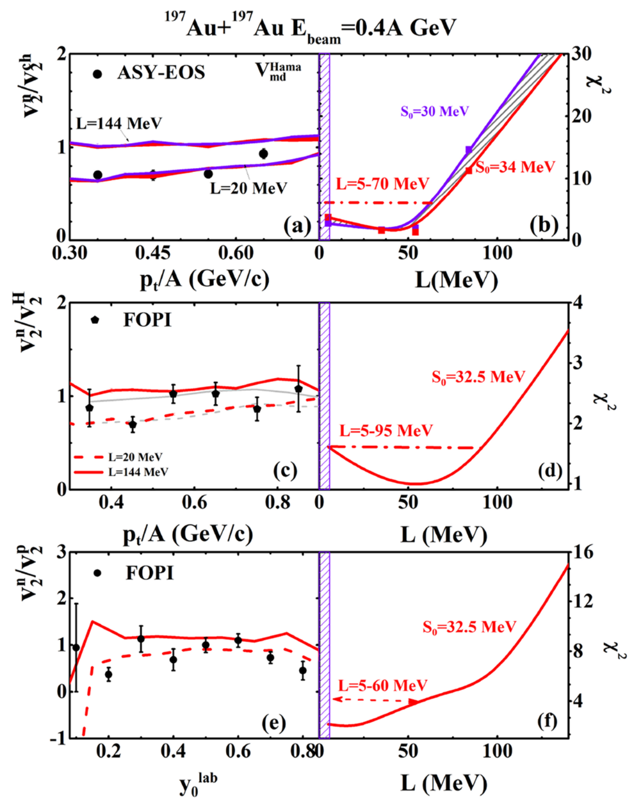

Fig. 5 (Color online) **a** $v_2^{\mathrm{n}}/v_2^{\mathrm{ch}}$ as a function of p_t/A for ^{197}Au+^{197}Au collisions with $L = 20$ MeV and 144 MeV at $S_0 = 30$ MeV (violet line) and $S_0 = 34$ MeV (red line). The black symbols represent the ASY-EOS experimental data. **c** $v_2^{\mathrm{n}}/v_2^{\mathrm{H}}$ as a function of p_t/A, **e** $v_2^{\mathrm{n}}/v_2^{\mathrm{p}}$ as a function of y_0^{lab} for ^{197}Au+^{197}Au collisions with $L = 20$ MeV and 144 MeV at $S_0 = 32.5$ MeV (red lines). The black symbols represent FOPI-LAND experimental data. **b** χ^2 of $v_2^{\mathrm{n}}/v_2^{\mathrm{ch}}$ as a function of L at $S_0 = 30$ MeV (violet line) and $S_0 = 34$ MeV (red line). **d, f** χ^2 of $v_2^{\mathrm{n}}/v_2^{\mathrm{H}}$, $v_2^{\mathrm{n}}/v_2^{\mathrm{p}}$ as a function of L at $S_0 = 32.5$ MeV (red line)

than that obtained in the soft symmetry energy case. This is because the emitted charged particles are mainly composed of free protons, which feel a stronger attractive interaction for the stiff symmetry energy case than that for the soft symmetry energy case at suprasaturation density.

Figure 4 shows the calculated results on the elliptic flow of neutrons, protons, and H isotopes. Panels (a) and (b) show $v_2^{\mathrm{n}}(p_t/A)$ and $v_2^{\mathrm{H}}(p_t/A)$, and panels (c) and (d) show $v_2^{\mathrm{n}}(y_0^{lab})$ and $v_2^{\mathrm{p}}(y_0^{lab})$. The red lines have the same meaning as those shown in Fig. 3. The gray lines represent the calculations using $v_{\mathrm{md}}^{\mathrm{Arnold}}$ in the previous UrQMD model [14]. The black symbols represent elliptic flow data from the FOPI-LAND experiment [14]. The calculations with $v_{\mathrm{md}}^{\mathrm{Hama}}$ can nearly reproduce the FOPI-LAND data. However, the strength of v_2^{n} and v_2^{H} is slightly overestimated at $p_t/A = 0.85$ GeV/c and an underestimation of the strength of v_2^{p} at $y_0^{lab} > 0.6$, which may be caused by isospin splitting of the proton and neutron effective masses [68, 69].

To single out the contributions of the isovector potential and cancel those of the isoscalar potentials, $v_2^{\mathrm{n}}/v_2^{\mathrm{ch}}$, $v_2^{\mathrm{n}}/v_2^{\mathrm{H}}$, and $v_2^{\mathrm{n}}/v_2^{\mathrm{p}}$ ratios were proposed to probe the symmetry energy. Figure 5a shows the calculations for $v_2^{\mathrm{n}}/v_2^{\mathrm{ch}}$ as a function of p_t/A obtained with $v_{\mathrm{md}}^{\mathrm{Hama}}$ and $\sigma_{NN\to N\Delta}^{\mathrm{Hub}}$. The lines represent the UrQMD calculations with $L = 20$ MeV (dash) and $L = 144$ MeV case (solid) at $S_0 = 30$ MeV (violet) and $S_0 = 34$ MeV (red). The lower calculation limit is $L = 5$ MeV represented by the rectangular box. The calculations show that $v_2^{\mathrm{n}}/v_2^{\mathrm{ch}}$ is sensitive to L at the low p_t region where the mean field plays a more important role. The $v_2^{\mathrm{n}}/v_2^{\mathrm{ch}}$ values obtained with the stiff symmetry energy cases are larger than that with the soft symmetry energy case, which is consistent with the results by using the UrQMD model [14, 16, 31], IBUU model [17], or TüQMD model [18, 54]. This behavior can be understood from Fig. 3c and d. By comparing the calculations of $v_2^{\mathrm{n}}/v_2^{\mathrm{ch}}$ with the ASY-EOS experimental data [31] represented by the symbols and doing a χ^2 analysis, one can find the parameter sets favored by data. Within the framework of UrQMD and setting $S_0 = 30 - 34$ MeV, the parameter sets with $L = 5 - 70$ MeV can describe the data.

Figure 5c and e depicts the calculated $v_2^{\mathrm{n}}/v_2^{\mathrm{H}}(p_t/A)$ and $v_2^{\mathrm{n}}/v_2^{\mathrm{p}}(y_0^{lab})$ results, respectively. The L dependence of the χ^2 value at $S_0 = 32.5$ MeV for $v_2^{\mathrm{n}}/v_2^{\mathrm{H}}$ and $v_2^{\mathrm{n}}/v_2^{\mathrm{p}}$

are presented in Fig. 5d and f. By comparing with the FOPI-LAND data [14] and conducting a χ^2 analysis, we obtain L constraints from $v_2^{\mathrm{n}}/v_2^{\mathrm{H}}(p_{\mathrm{t}}/A)$ in a broader range of L = 5–95 MeV, owing to the larger uncertainty in the $v_2^{\mathrm{n}}/v_2^{\mathrm{H}}(p_{\mathrm{t}}/A)$ data. The L constraints from $v_2^{\mathrm{n}}/v_2^{\mathrm{p}}(y_0^{\mathrm{lab}})$ calculations are L = 5–60 MeV, which is narrower than those from $v_2^{\mathrm{n}}/v_2^{\mathrm{ch}}(p_{\mathrm{t}}/A)$ and $v_2^{\mathrm{n}}/v_2^{\mathrm{H}}(p_{\mathrm{t}}/A)$ since the more pronounced sensitivity of the symmetry potential effects on free protons. As our calculations can reproduce the differential data of elliptic flow, it naturally expects that the ratios of integral value of the elliptical flow, i.e., $v_2^{\mathrm{n}}/v_2^{\mathrm{H}}$, $v_2^{\mathrm{n}}/v_2^{\mathrm{p}}$, and the difference $v_2^{\mathrm{n}} - v_2^{\mathrm{H}}$ $v_2^{\mathrm{n}} - v_2^{\mathrm{p}}$, can describe the experimental data.

The constraint by flow ratio and flow difference in this work is lower than those with the previous UrQMD model [31] or TüQMD model [27]. The discrepancy between our results and those of the previous UrQMD [31] is caused by using the different forms of v_{md} and K_0. In Ref. [31], $v_{\mathrm{md}}^{\mathrm{Arnold}}$ and $K_0 = 200$ MeV were used, and they provided a weaker repulsive force than that in our study. Consequently, the magnitude of the elliptic flow was underestimated. Consequently, their study required a more repulsive symmetry potential at high density, which has large L values. The difference between our results and TüQMD results [27] may be caused by using different K_0 and impact parameter ranges in calculations. In Ref. [27], they used $K_0 = 214$ MeV and the impact parameter $b < 7.5$ fm. In our case, $K_0 = 231$ MeV, the impact parameter is distributed from 0 to 10 fm, and the weight of the impact parameter has a Gaussian form, inferred from the experimental event selection [31]. Both lead to the L value constraints being higher than our study results. In addition, the different treatments for the medium effect of elastic cross sections and isovector neutron-proton effective mass splitting may also have some effects; however, understanding the difference requires further study.

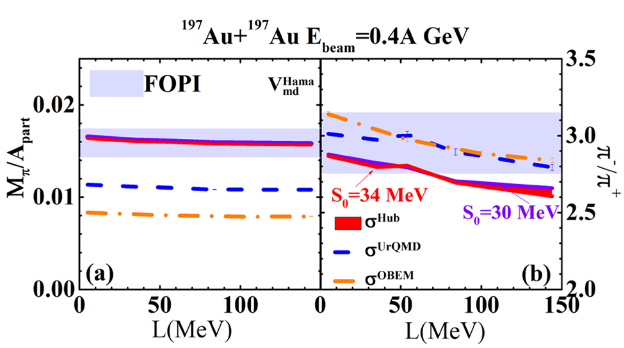

Fig. 6 (Color online) **a** M_π/A_{part}, and **b** π^-/π^+ as a function of L for ^{197}Au+^{197}Au collisions with $\sigma_{NN\to N\Delta}^{\mathrm{Hub}}$ at $S_0 = 30$ MeV (violet lines) and $S_0 = 34$ MeV (red lines), with $\sigma_{NN\to N\Delta}^{\mathrm{UrQMD}}$ (blue line) and $\sigma_{NN\to N\Delta}^{\mathrm{OBEM}}$ (orange line) at $S_0 = 32.5$ MeV. The shaded region is the FOPI data [67]

3.2 Pion productions and charged pion multiplicity ratios

Figure 6a shows the calculated pion multiplicity per participant M_π/A_{part} as a function of L with different $\sigma_{NN\to N\Delta}$ and symmetry energy forms. A_{part} is the number of nucleons in the participant, which constitutes 90% of the total mass of the system. The red and violet lines represent the calculations with $\sigma_{NN\to N\Delta}^{\mathrm{Hub}}$ at S_0 = 30 and 34 MeV, respectively. The orange and blue lines represent the results obtained using $\sigma_{NN\to N\Delta}^{\mathrm{OBEM}}$ and $\sigma_{NN\to N\Delta}^{\mathrm{UrQMD}}$ at S_0 = 32.5 MeV. The results obtained with $\sigma_{NN\to N\Delta}^{\mathrm{OBEM}}$ are lower than the data because the $\sigma_{NN\to N\Delta}^{\mathrm{OBEM}}$ is 50% lower than the $\sigma_{NN\to N\Delta}^{\mathrm{Hub}}$ at $E = 0.4A$ GeV. In this case, one may expect that an obvious threshold effect is required to enhance the production of pions to describe the data. The calculation obtained using $\sigma_{NN\to N\Delta}^{\mathrm{UrQMD}}$ underestimated M_π/A_{part} by approximately 30%, relative to the data. This discrepancy can be understood from the underestimation of the $NN \to N\Delta$ cross-section data using the default formula $\sigma_{NN\to N\Delta}^{\mathrm{UrQMD}}$, as shown in Fig. 2a. The surprising thing is that the results obtained with the $\sigma_{NN\to N\Delta}^{\mathrm{Hub}}$ fall into the data region since the $\sigma_{NN\to N\Delta}^{\mathrm{Hub}}$ enhances the cross sections by a factor of 8.56 at 0.4A GeV relative to the $\sigma_{NN\to N\Delta}^{\mathrm{UrQMD}}$. The above conclusion is not modified by using the different values of S_0 and L, i.e., in the range of $S_0 = 30, 34$ MeV and $L = 5-144$ MeV. Thus, only M_π/A_{part} cannot be used to distinguish between the different forms of symmetry energy.

In Fig. 6b, we present the calculated ratios π^-/π^+ as a function of L with different forms of $\sigma_{NN\to N\Delta}$ and S_0. These calculations indicate that π^-/π^+ is sensitive to L and $\sigma_{NN\to N\Delta}$. Using $\sigma_{NN\to N\Delta}^{\mathrm{UrQMD}}$ or $\sigma_{NN\to N\Delta}^{\mathrm{OBEM}}$ leads to fewer pions, but increase the values of π^-/π^+ which fall into the data region for $L = 5-144$ MeV. Even calculations with $\sigma_{NN\to N\Delta}^{\mathrm{UrQMD}}$ or $\sigma_{NN\to N\Delta}^{\mathrm{OBEM}}$ can reproduce the π^-/π^+ data (the blue and orange lines); however, one cannot make this conclusion because the pion multiplicity is underestimated relative to the data. For the calculations with $\sigma_{NN\to N\Delta}^{\mathrm{Hub}}$, the data of both M_π/A_{part} and π^-/π^+ can be reproduced with the $L = 5-70$ MeV and $S_0 = 30-34$ MeV parameter sets.

However, one should keep in mind that the integral observable, i.e., the pion multiplicity, is less influenced by pion potential due to the cancelation effects from pion potential and threshold effects [70]. To deeply understand the effect from pion-nucleon potential, a differential observable, such as the energy spectral of pion yields and charged pion rations or pionic flow, is suggested [30, 71] and it should be further studied in both the theoretical and experimental sides.

4 The symmetry energy constraints and its model dependence

4.1 The characteristic densities of pion and nucleonic flow observables

Before extracting the symmetry energy constraints at the suprasaturation density with collective flow and charged pion production, it is interesting to check the characteristic density probed by charged pion production and nucleonic flow observable, i.e., $\langle\rho\rangle^{\pi}_{\mathrm{char}}$ and $\langle\rho\rangle^{\mathrm{flow}}_{\mathrm{char}}$. The characteristic density of the pion observable is obtained by folding the compressed density with the pion production rate and the force acting on Δs in the spatiotemporal domain in our previous work [28], which showed that $\langle\rho\rangle^{\pi}_{\mathrm{char}}$ is approximately $1.5 \pm 0.5\ \rho_0$. This value was consistent with the results reported in Refs.[30, 72–76], but higher than the results in Ref. [77]. In this section, we investigate $\langle\rho\rangle^{\mathrm{flow}}_{\mathrm{char}}$ and discuss the recent symmetry energy constraints at $\langle\rho\rangle^{\mathrm{flow}}_{\mathrm{char}}$ and $\langle\rho\rangle^{\pi}_{\mathrm{char}}$.

For the collective flow of neutrons and charged particles, the idea to calculate the characteristic density $\langle\rho\rangle^{\mathrm{flow}}_{\mathrm{char}}$ is the same as $\langle\rho\rangle^{\pi}_{\mathrm{char}}$ in our previous work [28]; however, the weight was replaced by the momentum change of the nucleons. The momentum change in the nucleons during this time interval reflects the strength of the driving force for the collective motion of the emitted particles and can be used to understand the origins of v_1 and v_2.

In the following calculations, two kinds of momentum change of nucleons were used. One is the momentum change in the reaction plane, that is, $|\Delta p_x|$, which can be used to quantitatively describe the characteristic density probed by v_1. The corresponding characteristic density $\langle\rho\rangle^{\mathrm{flow}}_{\mathrm{char},|\Delta p_x|}$ is defined as

$$\langle\rho\rangle^{\mathrm{flow}}_{\mathrm{char},|\Delta p_x|} = \frac{\int_{t_0}^{t_1} \Sigma_i |\Delta p_x^i(t)/\Delta t| \rho_{\mathrm{c}}(t)\mathrm{d}t}{\int_{t_0}^{t_1} \Sigma_i |\Delta p_x^i(t)/\Delta t| \mathrm{d}t} \tag{8}$$

The other is the momentum change in the transverse direction, i.e., $|\Delta p_{\mathrm{t}}|$, which can be used to quantitatively describe that probed by v_2, and we calculate the $\langle\rho\rangle^{\mathrm{flow}}_{\mathrm{char},|\Delta p_{\mathrm{t}}|}$ as follows:

$$\langle\rho\rangle^{\mathrm{flow}}_{\mathrm{char},|\Delta p_{\mathrm{t}}|} = \frac{\int_{t_0}^{t_1} \Sigma_i |\Delta p_{\mathrm{t}}^i(t)/\Delta t| \rho_{\mathrm{c}}(t)\mathrm{d}t}{\int_{t_0}^{t_1} \Sigma_i |\Delta p_{\mathrm{t}}^i(t)/\Delta t| \mathrm{d}t}. \tag{9}$$

The summation over i runs over the nucleons belonging to the emitted nucleons and charged particles. For more details, $|\Delta p^i_{x/t}(t)/\Delta t| = |(p^i_{x/t}(t) - p^i_{x/t}(t-\Delta t))/\Delta t|$ is the change in the momentum of the nucleons during the time interval. The average central density $\rho_{\mathrm{c}}(t)$ was obtained in a spherical region centered at the c.m. of the system with a radius of 3.35 fm. This region represents the overlapping region in the semi-peripheral collisions of Au + Au.

Using Eqs. (8) and (9), the characteristic densities of the collective flow were obtained to be approximately $1.2 \pm 0.6\rho_0$. This is consistent with the characteristic densities obtained in Ref. [75] and Ref. [78]; however, it is smaller than the characteristic density obtained with pion observables.

Thus, by comparing the isospin-sensitive flow observable calculations $v_2^{\mathrm{n}}/v_2^{\mathrm{ch}}(p_{\mathrm{t}}/A)$, $v_2^{\mathrm{n}}/v_2^{\mathrm{H}}(p_{\mathrm{t}}/A)$, $v_2^{\mathrm{n}}/v_2^{\mathrm{p}}(y_0^{\mathrm{lab}})$, $v_2^{\mathrm{n}}/v_2^{\mathrm{H}}$, $v_2^{\mathrm{n}}/v_2^{\mathrm{p}}$, $v_2^{\mathrm{n}} - v_2^{\mathrm{H}}$, $v_2^{\mathrm{n}} - v_2^{\mathrm{p}}$, and the pion observables π^-/π^+ with the data, we can obtain the symmetry energy constraints at their characteristic densities, that is, $1.2 \pm 0.6\rho_0$ and $1.5 \pm 0.5\rho_0$.

4.2 The symmetry energy at characteristic densities and its model dependence

In Fig. 7a and b, we present the symmetry energy values at their characteristic densities, i.e., $S(1.2\rho_0)$ and $S(1.5\rho_0)$, obtained in this study (red symbols with errors). The uncertainties are the differences between the lower and upper boundaries of the favored symmetry energy parameter sets. The upper boundary of the symmetry energy was obtained with the symmetry energy with $(S_0, L) = (34,70)$ MeV, and the lower boundary was obtained with the symmetry energy with $(S_0, L) = (30, 5)$ MeV. For the historical constraints on the symmetry energy [14–16, 21–23, 25–31, 70, 79], we calculate the density dependence of symmetry energy according to the constraints given in previous studies. Subsequently, the values of $S(1.2\rho_0)$ and $S(1.5\rho_0)$ and their uncertainties were obtained in the same way. The results are represented by blue symbols with errors.

The $S(1.2\rho_0)$ values obtained in this study were between 30 and 38 MeV. This is slightly lower than the constraints from the analyses of elliptic flow ratios or elliptic flow differences using the previous version of the UrQMD [16, 31]

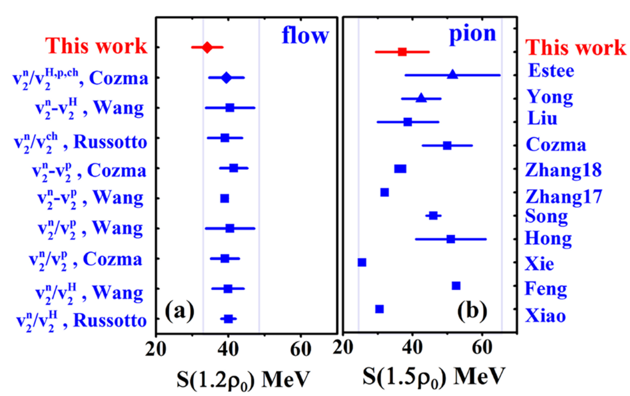

Fig. 7 **a** and **b** are the constraints of $S(1.2\rho_0)$ and $S(1.5\rho_0)$ in this study (red symbols) and from the previous study (blue symbols)

and TüQMD models [15, 18], which are in the 34–48 MeV range. The $S(1.5\rho_0)$ value obtained in this study ranged from $28-44\,\mathrm{MeV}$, which can overlap with the recent constraints by comparing SπRIT data with dcQMD [30] ($S(1.5\rho_0)=38-72\,\mathrm{MeV}$) and IBUU models [29] ($S(1.5\rho_0)=35-47\,\mathrm{MeV}$) within their uncertainties. Our results can also overlap with the previous constraints from the FOPI data by using the previous UrQMD version [28] by Liu et al, TüQMD [27] by Cozma et al, RVUU [26, 70] by Zhang et al, χBUU [79] by Zhang et al, pBUU [25] by Hong et al, and IBUU [21] by Xiao et al, but out of the constraints by using the isospin-dependent Boltzmann-Langevian (IBL) [23] model by Xie et al and the Lanzhou quantum molecular dynamics (LQMD) model [22] by Feng et al.

To quantitatively describe the theoretical uncertainties caused by the model dependence, a quantity,

$$\delta_{\mathrm{model}}(\rho^*)=\frac{S_{\max}(\rho^*)}{S_{\min}(\rho^*)}, \tag{10}$$

is adopted. $S_{\max}(\rho^*)$ and $S_{\min}(\rho^*)$ are the largest and smallest values of the symmetry energy constraints at ρ^* among the different models. The larger the model dependence, the larger the δ_{model} is. If there is no model dependence, δ_{model} will be one. For the symmetry energy constraints at $1.2\rho_0$ using the FOPI-LAND and ASY-EOS flow data, that is, $S(1.2\rho_0)$, the δ_{model} is 1.45. For the symmetry energy constraints at $1.5\rho_0$ using the FOPI and SπRIT pion data, that is, $S(1.5\rho_0)$, the δ_{model} is 2.75. These values are smaller than the model dependence described by the extrapolated symmetry energy at $3\rho_0$, that is, $S(3\rho_0)$, which is $\delta_{\mathrm{model}}(3\rho_0)=170$. This clearly indicates that simply extrapolating the symmetry energy constraints from the characteristic density to other densities may lead to a misunderstanding of the symmetry energy constraints via HICs.

4.3 Remarks on the symmetry energy constraints at 0.1–3.0 ρ_0

Notably, presenting the symmetry energy only at $1.2\rho_0$ and $1.5\rho_0$ is incomplete because the probed density region using flow and pion observables is in a wide density region, that is, in $1.2\pm0.6\rho_0$ for flow observables and $1.5\pm0.5\rho_0$ for pion observables. In Fig. 8a, we present the constrained symmetry energy in the flow characteristic density region (0.6–1.8ρ_0) as a pink shaded region, and the constraints in the pion characteristic density region (1.0–2.0ρ_0) with a violet shaded region. This completely overlaps with the constraints from the theoretical calculation using the chiral effective field theory (χEFT)[80] (green region); however, the uncertainty is larger than that from χEFT. Compared with the analyses of the SπRIT data obtained using dcQMD [30], the

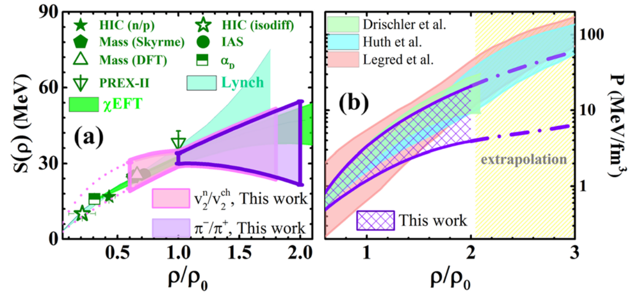

Fig. 8 (Color online) **a** The density dependence of symmetry energy constraints in this study at $1.2\pm0.6\rho_0$ region (wink region) and at the $1.5\pm0.5\rho_0$ region (violet region). Other constraints are obtained from Ref. [72] (cyan region) and Ref. [80] (green region). **b** The density dependence of the corresponding pressure of neutron star matter in this study (violet region) and the extrapolation (violet dash lines), and the pressure constraints of neutron star matter obtained by Drischler et al. [80] (green region), Legred et al. [87] (pink region), and Huth et al. [73] (cyan region)

symmetry energy constraint in the high-density region is relatively small. However, it can overlap with the uncertainty.

For symmetry energies below $0.6\rho_0$ and above $2\rho_0$, one can only infer the symmetry energy values by extrapolation because the symmetry energy information in these density regions is beyond the capability of the flow and pion observables at 0.4A GeV. The extrapolated symmetry energy below $0.6\rho_0$ is consistent with the results from the neutron to proton yield ratios in HICs (HIC(n/p)) [81], the isospin diffusion in HICs (HIC(isodiff)) [82], the nuclear mass calculated by the Skyrme energy-density functional (Skyrme-EDF[A12]) (Mass(Skyrme)) [83] and density functional theory (DFT) (Mass(DFT))[84], isobaric analog state (IAS) [85], and electric dipole polarization α_D[86], decoded by Lynch and Tsang in Ref. [72]. However, the uncertainties of the constraints using HICs in this study were larger than those of these observables. The extrapolated symmetry energy above $2\rho_0$ is weaker than that obtained from the neutron star by Drischler et al. [80], Legred et al. [87], and Huth et al. [73], as shown in Fig. 8b. This discrepancy may be related to the momentum-dependent symmetry potential uncertainties, which may provide the same symmetry energy density dependence but with different effects on the isospin-sensitive observables [46, 88–93]. Thus, investigating the form of the momentum-dependent symmetry potential is very important in HICs.

5 Summary and outlook

In summary, we investigated the influence of different momentum-dependent interactions, symmetry energy and $NN\to N\Delta$ cross sections on nucleonic and pion observables, such as $v_1^{\rm n}(p_{\rm t}/A)$, $v_1^{\rm ch}(p_{\rm t}/A)$, $v_2^{\rm n}(p_{\rm t}/A)$, $v_2^{\rm ch}(p_{\rm t}/A)$, $v_2^{\rm n}(p_{\rm t}/A)$, $v_2^{\rm H}(p_{\rm t}/A)$, $v_2^{\rm n}(y_0^{\rm lab})$, $v_2^{\rm p}(y_0^{\rm lab})$, $v_2^{\rm n}/v_2^{\rm ch}(p_{\rm t}/A)$, $v_2^{\rm n}/v_2^{\rm H}(p_{\rm t}/A)$, $v_2^{\rm n}/v_2^{\rm p}(y_0^{\rm lab})$, $v_2^{\rm n}/v_2^{\rm H}$, $v_2^{\rm n}/v_2^{\rm p}$, $v_2^{\rm n}-v_2^{\rm H}$, $v_2^{\rm n}-v_2^{\rm p}$, M_π, and π^-/π^+, using the UrQMD model for Au+Au collision at a beam energy of 0.4A GeV. Our results confirm that the elliptic flows of neutrons and charged particles, i.e., $v_2^{\rm n}$ and $v_2^{\rm ch}$, are sensitive to momentum-dependent interactions. The ASY-EOS and FOPI-LAND flow data favor calculations with strong momentum-dependent interactions, that is, $v_{\rm md}^{\rm Hama}$. However, calculations with $v_{\rm md}^{\rm Hama}$ underestimate the pion multiplicity by approximately 30% relative to FOPI data if the $\sigma_{NN\to N\Delta}^{\rm UrQMD}$ is adopted. Our calculations illustrate that the underestimation can be fixed by considering the accurate $NN\to N\Delta$ cross sections $\sigma_{NN\to N\Delta}^{\rm Hub}$ in the UrQMD model.

Furthermore, the symmetry energy constraints at the flow and pion characteristic densities were investigated using the updated UrQMD model. The characteristic density probed by the flow is approximately $1.2\rho_0$, which is smaller than the pion characteristic density of $1.5\rho_0$ [28]. By simultaneously describing the data of $v_2^{\rm n}/v_2^{\rm ch}(p_{\rm t}/A)$, $v_2^{\rm n}/v_2^{\rm H}(p_{\rm t}/A)$, $v_2^{\rm n}/v_2^{\rm p}(y_0^{\rm lab})$, $v_2^{\rm n}/v_2^{\rm p}$, $v_2^{\rm n}/v_2^{\rm H}$, $v_2^{\rm n}-v_2^{\rm p}$, $v_2^{\rm n}-v_2^{\rm H}$, and π^-/π^+ with UrQMD calculations, the favored effective interaction parameter sets are obtained and we got the $S(1.2\rho_0)=34\pm4\,$MeV and $S(1.5\rho_0)=36\pm8\,$MeV. The extrapolated values of L in this work are in $5-70\,$MeV within 2σ uncertainty for $S_0=30-34\,$MeV, which is below the analysis of the PREX-II results with a specific class of relativistic energy density functional [94], but is consistent with the constraint from the charged radius of ^{54}Ni [95], resulting from combining the astrophysical data with PREX-II and χEFT [96], and from the SπRIT pion data for the Sn+Sn collision at 0.27A GeV [30].

For the model dependence of the symmetry energy constraints, our calculations show that the strengths of the model dependence among the different transport models are 1.45 and 2.75 for the symmetry energy at the flow and pion characteristic density, respectively. These values are obviously smaller than the strength of the model dependence described by the symmetry energy at three times normal density, which is 170.

Finally, simultaneously describing the ASY-EOS and FOPI data provides a rigorous limit on the UrQMD model and a solid foundation to further understand the effects of unsolved physics problems, such as the threshold effect, the pion potential, and the momentum-dependent symmetry potential.

Notably, the discrepancies in $v_2^{\rm n}$ and $v_2^{\rm p}$ at high $p_{\rm t}$ and rapidity relative to the data demonstrate the importance of the momentum dependence of the symmetry potential, as mentioned in Refs. [68, 69, 77], which should be investigated using the momentum and rapidity distributions of the nucleonic and pionic probes in the future. Another important direction for developing the transport model and limiting its uncertainties is describing the nucleonic and pionic flow observables and their spectra at subthreshold energies and above 1 GeV/u. This will help to further understand the pion production mechanism and provide the symmetry energy constraints twice beyond the normal density with HICs.

Acknowledgements The authors acknowledge the support of Huzhou University for the computing server C3S2 and are grateful for the transport model and symmetry energy constraint discussions at the TMEP weekly meeting.

Author contributions All authors contributed to the study conception and design. Material preparation, data collection and analysis were performed by Yang-Yang Liu, Yong-Jian Wang, Qing-Feng Li, and Ying-Xun Zhang. The first draft of the manuscript was written by Yang-Yang Liu and all authors commented on previous versions of the manuscript. All authors read and approved the final manuscript.

Data availability The data that support the findings of this study are openly available in Science Data Bank at https://cstr.cn/31253.11.sciencedb.j00186.00428 and https://www.doi.org/10.57760/sciencedb.j00186.00428.

References

1. B.A. Li, L.W. Chen, C.M. Ko, Recent progress and new challenges in isospin physics with heavy-ion reactions. Phys. Rept. **464**, 113–281 (2008). https://doi.org/10.1016/j.physrep.2008.04.005
2. W.D. Tian, Y.G. Ma, X.Z. Cai et al., Isospin and symmetry energy study in nuclear EOS. Sci. China Phys. Mech. Astron. **54**, 141–148 (2011). https://doi.org/10.1007/s11433-011-4424-8
3. S.H. Cheng, J. Wen, L.G. Cao et al., Neutron skin thickness of ^{90}Zr and symmetry energy constrained by charge exchange spin-dipole excitations. Chin. Phys. C **47**, 024102 (2023). https://doi.org/10.1088/1674-1137/aca38e
4. R. An, S. Sun, L.G. Cao, F.S. Zhang, Constraining nuclear symmetry energy with the charge radii of mirror-pair nuclei. Nucl. Sci. Tech. **34**, 119 (2023). https://doi.org/10.1007/s41365-023-01269-1
5. C.J. Horowitz, E.F. Brown, Y. Kim et al., A way forward in the study of the symmetry energy: experiment, theory, and observation. J. Phys. G **41**, 093001 (2014). https://doi.org/10.1088/0954-3899/41/9/093001
6. J.M. Lattimer, M. Prakash, The physics of neutron stars. Science **304**, 536–542 (2004). https://doi.org/10.1126/science.1090720
7. A.W. Steiner, J.M. Lattimer, E.F. Brown, The equation of state from observed masses and radii of neutron stars. Astrophys. J. **722**(1), 33 (2010). https://doi.org/10.1088/0004-637X/722/1/33
8. N.B. Zhang, B.A. Li, Astrophysical constraints on a parametric equation of state for neutron-rich nucleonic matter. Nucl. Sci. Tech. **29**, 178 (2018). https://doi.org/10.1007/s41365-018-0515-9
9. J.F. Xu, C.J. Xia, Z.Y. Lu et al., Symmetry energy of strange quark matter and tidal deformability of strange quark stars. Nucl. Sci. Tech. **33**, 143 (2022). https://doi.org/10.1007/s41365-022-01130-x
10. X.F. Luo, Q. Wang, N. Xu, P. Zhuang (Eds.) Properties of QCD matter at high Baryon densities. (Springer, 2022). https://doi.org/10.1007/978-981-19-4441-3

11. P. Danielewicz, R. Lacey, W.G. Lynch, Determination of the equation of state of dense matter. Science **298**, 1592–1596 (2002). https://doi.org/10.1126/science.1078070
12. J. Carlson, M.P. Carpenter, R. Casten et al., White paper on nuclear astrophysics and low-energy nuclear physics, Part 2: low-energy nuclear physics. Progress Particle Nucl. Phys. **94**, 68–124 (2017). https://doi.org/10.1016/j.ppnp.2016.11.002
13. A. Bracco, The NuPECC long range plan 2017: perspectives in nuclear physics. Europhys. News **48**, 21–24 (2017). https://doi.org/10.1051/epn/2017403
14. P. Russotto, P.Z. Wu, M. Zoric et al., Symmetry energy from elliptic flow in ^{197}Au+^{197}Au. Phys. Letter. B **697**(5), 471–476 (2011). https://doi.org/10.1016/j.physletb.2011.02.033
15. M.D. Cozma, Y. Leifels, W. Trautmann et al., Toward a model-independent constraint of the high-density dependence of the symmetry energy. Phys. Rev. C **88**(4), 044912 (2013). https://doi.org/10.1103/PhysRevC.88.044912
16. Y.J. Wang, C.C. Guo, Q.F. Li et al., Constraining the high-density nuclear symmetry energy with the transverse-momentum dependent elliptic flow. Phys. Rev. C **89**(4), 044603 (2014). https://doi.org/10.1103/PhysRevC.89.044603
17. G.C. Yong, Cross-checking the symmetry energy at high densities. Phys. Rev. C **93**, 044610 (2016). https://doi.org/10.1103/PhysRevC.93.044610
18. M.D. Cozma, Feasibility of constraining the curvature parameter of the symmetry energy using elliptic flow data. Eur. Phys. J. A **54**, 40 (2018). https://doi.org/10.1140/epja/i2018-12470-1
19. B.A. Li, Probing the high density behavior of nuclear symmetry energy with high-energy heavy ion collisions. Phys. Rev. Lett. **88**, 192701 (2002). https://doi.org/10.1103/PhysRevLett.88.192701
20. B.A. Li, High density behavior of nuclear symmetry energy and high-energy heavy ion collisions. Nucl. Phys. A **708**, 365–390 (2002). https://doi.org/10.1016/S0375-9474(02)01018-7
21. Z.G. Xiao, B.A. Li, L.W. Chen et al., Circumstantial evidence for a soft nuclear symmetry energy at suprasaturation densities. Phys. Rev. Lett. **102**, 062502 (2009). https://doi.org/10.1103/PhysRevLett.102.062502
22. Z.Q. Feng, G.M. Jin, Probing high-density behavior of symmetry energy from pion emission in heavy-ion collisions. Phys. Lett. B **683**, 140–144 (2010). https://doi.org/10.1016/j.physletb.2009.12.006
23. W.J. Xie, J. Su, L. Zhu et al., Symmetry energy and pion production in the Boltzmann–Langevin approach. Phys. Lett. B **718**, 1510–1514 (2013). https://doi.org/10.1016/j.physletb.2012.12.021
24. W. Xie, F. Zhang, Probing the density dependence of the symmetry energy with central heavy ion collisions. Nucl. Sci. Tech. **24**, 050502 (2013). https://doi.org/10.13538/j.1001-8042/nst.2013.05.002
25. J. Hong, P. Danielewicz, Subthreshold pion production within a transport description of central Au + Au collisions. Phys. Rev. C **90**(2), 024605 (2014). https://doi.org/10.1103/PhysRevC.90.024605
26. T. Song, C.M. Ko, Modifications of the pion-production threshold in the nuclear medium in heavy ion collisions and the nuclear symmetry energy. Phys. Rev. C **91**(1), 014901 (2015). https://doi.org/10.1103/PhysRevC.91.014901
27. M.D. Cozma, The impact of energy conservation in transport models on the π^-/π^+ multiplicity ratio in heavy-ion collisions and the symmetry energy. Phys. Lett. B **753**, 166–172 (2016). https://doi.org/10.1016/j.physletb.2015.12.015
28. Y.Y. Liu, Y.J. Wang, Y. Cui et al., Insights into the pion production mechanism and the symmetry energy at high density. Phys. Rev. C **103**, 014616 (2021). https://doi.org/10.1103/PhysRevC.103.014616
29. G.C. Yong, Symmetry energy extracted from the SπRIT pion data in Sn+Sn systems. Phys. Rev. C **104**, 014613 (2021). https://doi.org/10.1103/PhysRevC.104.014613
30. J. Estee, W.G. Lynch, C.Y. Tsang et al., Probing the symmetry energy with the spectral pion ratio. Phys. Rev. Lett. **126**(16), 162701 (2021). https://doi.org/10.1103/PhysRevLett.126.162701
31. P. Russotto, S. Gannon, S. Kupny et al., Results of the ASY-EOS experiment at GSI: the symmetry energy at suprasaturation density. Phys. Rev. C **94**(3), 034608 (2016). https://doi.org/10.1103/PhysRevC.94.034608
32. Y.J. Wang, Q.F. Li, Application of microscopic transport model in the study of nuclear equation of state from heavy ion collisions at intermediate energies. Front. Phys. **15**, 44302 (2020). https://doi.org/10.1007/s11467-020-0964-6
33. B.A. Li, X. Han, Constraining the neutron-proton effective mass splitting using empirical constraints on the density dependence of nuclear symmetry energy around normal density. Phys. Lett. B **727**, 276–281 (2013). https://doi.org/10.1016/j.physletb.2013.10.006
34. M. Oertel, M. Hempel, T. Klähn et al., Equations of state for supernovae and compact stars. Rev. Mod. Phys. **89**(1), 015007 (2017). https://doi.org/10.1103/RevModPhys.89.015007
35. Y.X. Zhang, M. Liu, C.J. Xia et al., Constraints on the symmetry energy and its associated parameters from nuclei to neutron stars. Phys. Rev. C **101**(3), 034303 (2020). https://doi.org/10.1103/PhysRevC.101.034303
36. G. Jhang, J. Estee, J. Barney et al., Symmetry energy investigation with pion production from Sn+Sn systems. Phys. Lett. B **813**, 136016 (2021). https://doi.org/10.1016/j.physletb.2020.136016
37. Y.X. Zhang, Y.J. Wang, M. Colonna et al., Comparison of heavy-ion transport simulations: collision integral in a box. Phys. Rev. C **97**(3), 034625 (2018). https://doi.org/10.1103/PhysRevC.97.034625
38. A. Ono, J. Xu, M. Colonna et al., Comparison of heavy-ion transport simulations: collision integral with pions and Δ resonances in a box. Phys. Rev. C **100**(4), 044617 (2019). https://doi.org/10.1103/PhysRevC.100.044617
39. M. Colonna, Y.X. Zhang, Y.J. Wang et al., Comparison of heavy-ion transport simulations: mean-field dynamics in a box. Phys. Rev. C **104**(2), 024603 (2021). https://doi.org/10.1103/PhysRevC.104.024603
40. S.A. Bass, M. Belkacem, M. Bleicher et al., Microscopic models for ultrarelativistic heavy ion collisions. Prog. Part. Nucl. Phys. **41**, 255–369 (1998). https://doi.org/10.1016/S0146-6410(98)00058-1
41. M. Bleicher, E. Zabrodin, C. Spieles et al., Relativistic hadron-hadron collisions in the ultra-relativistic quantum molecular dynamics model. J. Phys. G Nucl. Part. Phys. **25**(9), 1859 (1999). https://doi.org/10.1088/0954-3899/25/9/308
42. L.G. Arnold, B.C. Clark, E.D. Cooper et al., Energy dependence of the p-^{40}Ca optical potential: a Dirac equation perspective. Phys. Rev. C **25**(2), 936–940 (1982). https://doi.org/10.1103/PhysRevC.25.936
43. S. Hama, B.C. Clark, E.D. Cooper et al., Global Dirac optical potentials for elastic proton scattering from heavy nuclei. Phys. Rev. C **41**, 2737–2755 (1990). https://doi.org/10.1103/PhysRevC.41.2737
44. C. Hartnack, J. Aichelin, New parametrization of the optical potential. Phys. Rev. C **49**, 2801–2804 (1994). https://doi.org/10.1103/PhysRevC.49.2801
45. A. Bonasera, F. Gulminelli, J. Molitoris, The Boltzmann equation at the borderline: a decade of Monte Carlo simulations of a quantum kinetic equation. Phys. Rept. **243**, 1–124 (1994). https://doi.org/10.1016/0370-1573(94)90108-2
46. B.A. Li, C.B. Das, S. Das Gupta et al., Effects of momentum dependent symmetry potential on heavy ion collisions induced by

neutron rich nuclei. Nucl. Phys. A **735**, 563–584 (2004). https://doi.org/10.1016/j.nuclphysa.2004.02.016
47. L.W. Chen, C.M. Ko, B.A. Li et al., Probing isospin- and momentum-dependent nuclear effective interactions in neutron-rich matter. Eur. Phys. J. A **50**, 29 (2014). https://doi.org/10.1140/epja/i2014-14029-6
48. F. Zhang, G.C. Yong, Effects of high-momentum tail of nucleon momentum distribution on initiation of cluster production in heavy-ion collisions at intermediate energies. Phys. Rev. C **106**, 054603 (2022). https://doi.org/10.1103/PhysRevC.106.054603
49. M. Isse, A. Ohnishi, N. Otuka et al., Mean-field effects on collective flows in high-energy heavy-ion collisions from AGS to SPS energies. Phys. Rev. C **72**, 064908 (2005). https://doi.org/10.1103/PhysRevC.72.064908
50. Q.-F. Li, M. Bleicher, A Model comparison of resonance lifetime modifications, a soft equation of state and non-Gaussian effects on pi-pi correlations at FAIR/AGS energies. J. Phys. G **36**, 015111 (2009). https://doi.org/10.1088/0954-3899/36/1/015111
51. O. Buss, T. Gaitanos, K. Gallmeister et al., Transport-theoretical description of nuclear reactions. Phys. Rept. **512**, 1–124 (2012). https://doi.org/10.1016/j.physrep.2011.12.001
52. N. Ikeno, A. Ono, Y. Nara, A. Ohnishi, Probing neutron-proton dynamics by pions. Phys. Rev. C **93**(4), 044612 (2016). https://doi.org/10.1103/PhysRevC.93.044612
53. Y. Nara, T. Maruyama, H. Stoecker, Momentum-dependent potential and collective flows within the relativistic quantum molecular dynamics approach based on relativistic mean-field theory. Phys. Rev. C **102**(2), 024913 (2020). https://doi.org/10.1103/PhysRevC.102.024913
54. M.D. Cozma, M.B. Tsang, In-medium Δ(1232) potential, pion production in heavy-ion collisions and the symmetry energy. Eur. Phys. J. A **57**(11), 309 (2021). https://doi.org/10.1140/epja/s10050-021-00616-3
55. V. Flaminio, W.G. Moorhead, D.R.0. Morrison, N. Rivoire, CERN-HERA-84-01. Geneva Report CERN-HERA-84-01 (1984)
56. Y. Cui, Y.X. Zhang, Z.X. Li, Δ-mass dependence of the M-matrix in the calculation of N $\Delta \rightarrow$ NN cross sections. Chin. Phys. C **44**(2), 024106 (2020). https://doi.org/10.1088/1674-1137/44/2/024106
57. Y. Zhang, N. Wang, Q.-F. Li et al., Progress of quantum molecular dynamics model and its applications in heavy ion collisions. Front. Phys. **15**, 54301 (2020). https://doi.org/10.1007/s11467-020-0961-9
58. G. Ferini, M. Colonna, T. Gaitanos et al., Aspects of particle production in charge asymmetric matter. Nucl. Phys. A **762**, 147–166 (2005). https://doi.org/10.1016/j.nuclphysa.2005.08.007
59. Q.F. Li, Z. Li, S. Soff et al., Probing the density dependence of the symmetry potential at low and high densities. Phys. Rev. C **72**, 034613 (2005). https://doi.org/10.1103/PhysRevC.72.034613
60. B.A. Li, Symmetry potential of Δ(1232) resonance and its effects on the π^-/π^+ ratio in heavy-ion collisions near the pion-production threshold. Phys. Rev. C **92**, 034603 (2015). https://doi.org/10.1103/PhysRevC.92.034603
61. S. Huber, J. Aichelin, Production of Delta and N* resonances in the one boson exchange model. Nucl. Phys. A **573**, 587–625 (1994). https://doi.org/10.1016/0375-9474(94)90232-1
62. A. Baldini, V. Flaminio, W.G. Moorhead et al., edited by H. Schopper, Total cross-sections for reactions of high energy particles (Including Elastic, Topological, Inclusive and Exclusive Reactions). Landolt-Boernstei–Group I Elementary Particles, Nuclei and Atoms, vol. 12a (Springer, 1988). https://doi.org/10.1007/b33548
63. P. Danielewicz, Determination of the mean field momentum dependence using elliptic flow. Nucl. Phys. A **673**, 375–410 (2000). https://doi.org/10.1016/S0375-9474(00)00083-X
64. J.D. Frankland, D. Gruyer, E. Bonnet et al., Model independent reconstruction of impact parameter distributions for intermediate energy heavy ion collisions. Phys. Rev. C **104**(3), 034609 (2021). https://doi.org/10.1103/PhysRevC.104.034609
65. L. Li, Y. Zhang, Z. Li et al., Impact parameter smearing effects on isospin sensitive observables in heavy ion collisions. Phys. Rev. C **97**, 044606 (2018). https://doi.org/10.1103/PhysRevC.97.044606
66. X. Chen, L. Li, Y. Cui, J. Yang, Z. Li, Y. Zhang, Bayesian reconstruction of impact parameter distributions from two observables for intermediate energy heavy ion collisions. Phys. Rev. C **108**, 034613 (2023). https://doi.org/10.1103/PhysRevC.108.034613
67. W. Reisdorf et al., Systematics of central heavy ion collisions in the 1*A* GeV regime. Nucl. Phys. A **848**, 366–427 (2010). https://doi.org/10.1016/j.nuclphysa.2010.09.008
68. Z.-Q. Feng, Effective mass splitting of neutron and proton and isospin emission in heavy-ion collisions. Nucl. Phys. A **878**, 3–13 (2012). https://doi.org/10.1016/j.nuclphysa.2012.01.014
69. V. Giordano, M. Colonna, M. Di Toro et al., Isospin emission and flows at high baryon densities: a test of the symmetry potential. Phys. Rev. C **81**, 044611 (2010). https://doi.org/10.1103/PhysRevC.81.044611
70. Z. Zhang, C.M. Ko, Medium effects on pion production in heavy ion collisions. Phys. Rev. C **95**(6), 064604 (2017). https://doi.org/10.1103/PhysRevC.95.064604
71. Y.Y. Liu, Y. Wang, Q. Li et al., Collective flows of pions in Au+Au collisions at energies 1.0 and 1.5 GeV/nucleon. Phys. Rev. C **97**, 034602 (2018). https://doi.org/10.1103/PhysRevC.97.034602
72. W.G. Lynch, M.B. Tsang, Decoding the density dependence of the nuclear symmetry energy. Phys. Lett. B **830**, 137098 (2022). https://doi.org/10.1016/j.physletb.2022.137098
73. S. Huth, P.T.H. Pang, I. Tews et al., Constraining neutron-star matter with microscopic and macroscopic collisions. Nature **606**, 276–280 (2022). https://doi.org/10.1038/s41586-022-04750-w
74. P. Russotto, S. Gannon, S. Kupny et al., Results of ASY-EOS experiment at GSI: symmetric energy at suprasaturation density. Phys. Rev. C **94**, 034608 (2016). https://doi.org/10.1103/PhysRevC.94.034608
75. A. Le Fèvre, Y. Leifels, W. Reisdorf et al., Constraining the nuclear matter equation of state around twice saturation density. Nucl. Phys. A **945**, 112–133 (2016). https://doi.org/10.1016/j.nuclphysa.2015.09.015
76. P. Russotto, M.D. Cozma, E. De Filippo et al., Studies of the equation-of-state of nuclear matter by heavy-ion collisions at intermediate energy in the multimessenger era: A review focused on GSI results. Riv. Nuovo Cim. **46**, 1–70 (2023). https://doi.org/10.1007/s40766-023-00039-4
77. Z.Q. Feng, Nuclear dynamics and particle production near threshold energies in heavy-ion collisions. Nucl. Sci. Tech. **29**, 40 (2018). https://doi.org/10.1007/s41365-018-0379-z
78. B. Gao, Y. Wang, Z. Gao et al., Elliptic flow in heavy-ion collisions at intermediate energy: role of impact parameter, mean field potential, and collision term. Phys. Lett. B **838**, 137685 (2023). https://doi.org/10.1016/j.physletb.2023.137685
79. Z. Zhang, C.M. Ko, Pion production in a transport model based on mean fields from chiral effective field theory. Phys. Rev. C **98**, 054614 (2018). https://doi.org/10.1103/PhysRevC.98.054614
80. C. Drischler, R.J. Furnstahl, J.A. Melendez et al., How well do we know the neutron-matter equation of state at the densities inside neutron stars? A Bayesian approach with correlated uncertainties. Phys. Rev. Lett. **125**(20), 202702 (2020). https://doi.org/10.1103/PhysRevLett.125.202702
81. P. Morfouace, C.Y. Tsang, Y. Zhang et al., Constraining the symmetry energy with heavy-ion collisions and Bayesian analyses. Phys. Lett. B **799**, 135045 (2019). https://doi.org/10.1016/j.physletb.2019.135045

82. M.B. Tsang, Y. Zhang, P. Danielewicz et al., Constraints on the density dependence of the symmetry energy. Phys. Rev. Lett. **102**, 122701 (2009). https://doi.org/10.1103/PhysRevLett.102.122701
83. B.A. Brown, Constraints on the Skyrme equations of state from properties of doubly magic nuclei. Phys. Rev. Lett. **111**(23), 232502 (2013). https://doi.org/10.1103/PhysRevLett.111.232502
84. M. Kortelainen, J. McDonnell, W. Nazarewicz et al., Nuclear energy density optimization: large deformations. Phys. Rev. C **85**, 024304 (2012). https://doi.org/10.1103/PhysRevC.85.024304
85. P. Danielewicz, P. Singh, J. Lee, Symmetry energy III: Isovector skins. Nucl. Phys. A **958**, 147–186 (2017). https://doi.org/10.1016/j.nuclphysa.2016.11.008
86. Z. Zhang, L.-W. Chen, the electric dipole polarizability in ^{208}Pb as a probe of the symmetry energy and neutron matter around $\rho_0/3$. Phys. Rev. C **92**(3), 031301 (2015). https://doi.org/10.1103/PhysRevC.92.031301
87. I. Legred, K. Chatziioannou, R. Essick et al., Impact of the PSR J0740+6620 radius constraint on the properties of high-density matter. Phys. Rev. D **104**(6), 063003 (2021). https://doi.org/10.1103/PhysRevD.104.063003
88. J. Rizzo, M. Colonna, M. Di Toro et al., Transport properties of isospin effective mass splitting. Nucl. Phys. A **732**, 202–217 (2004). https://doi.org/10.1016/j.nuclphysa.2003.11.057
89. B.A. Li, L.W. Chen, Neutron-proton effective mass splitting in neutron-rich matter and its impacts on nuclear reactions. Mod. Phys. Lett. A **30**, 1530010 (2015). https://doi.org/10.1142/S0217732315300104
90. W.J. Xie, Z.Q. Feng, J. Su et al., Probing the momentum-dependent symmetry potential via nuclear collective flows. Phys. Rev. C **91**, 054609 (2015). https://doi.org/10.1103/PhysRevC.91.054609
91. H.Y. Kong, Y. Xia, J. Xu et al., Reexamination of the neutron-to-proton-ratio puzzle in intermediate-energy heavy-ion collisions. Phys. Rev. C **91**, 047601 (2015). https://doi.org/10.1103/PhysRevC.91.047601
92. Y. Zhang, M.B. Tsang, Z. Li et al., Constraints on nucleon effective mass splitting with heavy ion collisions. Phys. Lett. B **732**, 186–190 (2014). https://doi.org/10.1016/j.physletb.2014.03.030
93. J.P. Yang, X. Chen, Y. Cui et al., Extended Skyrme momentum-dependent potential in asymmetric nuclear matter and transport models. Phys. Rev. C **109**, 054624 (2024). https://doi.org/10.1103/PhysRevC.109.054624
94. B.T. Reed, F.J. Fattoyev, C.J. Horowitz et al., Implications of PREX-2 on the equation of state of neutron-rich matter. Phys. Rev. Lett. **126**, 172503 (2021). https://doi.org/10.1103/PhysRevLett.126.172503
95. S.V. Pineda et al., Charge radius of neutron-deficient ^{54}Ni and symmetry energy constraints using the difference in mirror pair charge radii. Phys. Rev. Lett. **127**(18), 182503 (2021). https://doi.org/10.1103/PhysRevLett.127.182503
96. R. Essick, I. Tews, P. Landry et al., Astrophysical constraints on the symmetry energy and the neutron skin of ^{208}Pb with minimal modeling assumptions. Phys. Rev. Lett. **127**(19), 192701 (2021). https://doi.org/10.1103/PhysRevLett.127.192701